THE JOURNAL OF PHYSICAL CHEMISTRY C
A JOURNAL OF THE AMERICAN CHEMICAL SOCIETY

pubs.acs.org/JPCC

Article

Proton Donors Influence Nitrogen Adsorption in Lithium-Mediated Electrochemical Ammonia Synthesis

Victor Azumah, Lance Kavalsky, and Venkatasubramanian Viswanathan*

Cite This: J. Phys. Chem. C 2025, 129, 2488−2501

Read Online

ACCESS | Metrics & More | Article Recommendations | Supporting Information

ABSTRACT: Lithium-mediated electrochemical ammonia synthesis (LiMEAS) has recently shown promise toward efficient electrochemical ammonia production. This process relies on the formation of a lithium nitride film which is subsequently protonated to release ammonia. Designing the electrolyte for this technology requires the selection of a proton donor. In this work, we perform a first-principles analysis to investigate the initial step of nitride formation considering 30 different proton donors (PD). As a baseline, modeling nitrogen on a lithium surface without a PD, we observe that N_2 does not spontaneously dissociate on the lithium surface. However, explicitly introducing a PD into the system results in five unique recurring nitrogen configurations on the lithium slab: (1) embedded, (2) adsorbed, (3) standing, (4) buried, and (5) transferred states. We show that these PD-induced states possess an elongated N−N bond and adsorb more strongly on lithium. Using charge analysis, we show that the charge transferred onto these states strongly correlates with the change in their bond length, a crucial parameter for nitrogen dissociation. These results suggest a more involved role of the PD in the initial stages of nitride formation, and motivate greater consideration for their impact on the LiMEAS pathway.

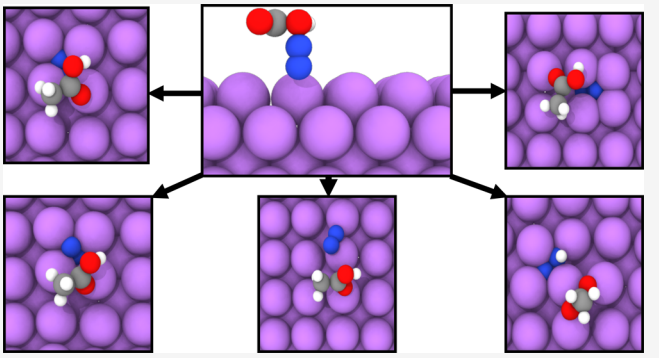

INTRODUCTION

Ammonia production accounts for 1−2% of global greenhouse gas emissions due to its use of the energy intensive Haber-Bosch process, which has been targeted for electrification.[1−10] Searching for a strategy to facilitate efficient green synthesis of ammonia, lithium-mediated electrochemical ammonia synthesis (LiMEAS) has recently demonstrated promise by consistently achieving current efficiencies above 60% with high ammonia production yields.[11−14] This LiMEAS approach can be described as a three-step process involving: (i) electrodeposition of lithium onto an electrode (eq 1), (ii) formation of a lithium nitride film via nitrogen dissociation (eq 2), and (iii) hydrogenation of the nitrogen by a proton donor to release ammonia with the recovery of lithium ions at the end (eq 3). The overall reaction is an electrochemical process given by eq 4, highlighting lithium's catalytic role.

$$Li^+(aq) + e^- \rightarrow Li(s) \quad (1)$$

$$3Li(s) + \frac{1}{2}N_2(g) \rightarrow Li_3N(s) \quad (2)$$

$$Li_3N(s) + 3H^+(aq) \rightarrow 3Li^+(aq) + NH_3(g) \quad (3)$$

$$\frac{1}{2}N_2(g) + 3(H^+ + e^-) \rightarrow NH_3(g) \quad (4)$$

A proof-of-concept was recently demonstrated in a full cell setup.[15−18] Key to this process is lithium's ability to dissociate the nitrogen triple bond at near-ambient conditions.[19−23] This lithium-induced dissociation of nitrogen is a chemical process that is competitive with the hydrogen evolution reaction, the main side reaction leading to low faradaic efficiencies in the system.[24,25] These advances in activity and selectivity give LiMEAS an advantage over previous electrochemical ammonia synthesis methods which have been plagued by materials design challenges.[14,22,23,25−30] However, despite the high observed current and faradaic efficiencies from LiMEAS, obstacles remain to improve cyclability and yield.[11,12,31,32]

To better understand the LiMEAS system, fundamental investigations into the dynamics of the lithium metal−electrolyte interface are invaluable.[13,33,34] This electrochemical interface is reminiscent of the anode in lithium metal batteries, where components of the electrolyte can react with the surface forming a solid-electrolyte interphase (SEI) that has significant impacts on battery performance.[35−42] In this LiMEAS case,

Received: December 2, 2024
Revised: January 13, 2025
Accepted: January 17, 2025
Published: January 28, 2025

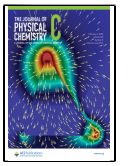

https://doi.org/10.1021/acs.jpcc.4c08138
J. Phys. Chem. C 2025, 129, 2488−2501

unfavorable interactions with electrolyte components inhibit the reaction of nitrogen with the electrodeposited lithium by slowing, or completely blocking, its diffusion to the surface.[31,32,38,39,42−45] Highlighting the parallels between these domains, in batteries, fluorinated solvents were shown to form a favorable SEI composition, whereas for LiMEAS, fluoride-based salts were shown to form uniform SEI interfaces that improved nitrogen transport.[12,13,37] Thus, as with lithium metal batteries, several system component interactions may coexist leading to a range in overall performance.

Considering the components of an electrolyte designed for LiMEAS, the proton donor (PD) identity is important as it has been shown to have a nontrivial effect on interface morphology.[34] Specifically, the Kamlet−Taft (KT) parameters have been highlighted for their correlation to nitrogen reduction activity.[46] To this point, previous work exploring the mechanistic importance of PD behaviors on the system showed that their positive effect on interface morphology increased Faradaic efficiency up to a threshold after which excess hydrogen evolution began to occur adversely affecting ammonia synthesis.[47] Initially assumed to act only as a source of protons for nitrogen reduction, the PD was generally considered a design parameter for controlling hydrogen evolution by tuning its availability and dissociation.[15,16] Work along these lines has involved the explorations of proton shuttles[11] and proton donors of intermediate dissociation strength.[48]

Recent findings on the PD's effect on interfacial morphology suggest the PD may interact with other system components beyond providing protons.[32,34,47] In particular, its role in the formation of lithium nitride remains unclear.

In this work, we explore how the presence of a PD dictates the initial stages of nitride formation for LiMEAS. Using density functional theory (DFT) calculations, we show that in the absence of the PD, nitrogen does not spontaneously dissociate into a nitride, and nitrogen configurations on lithium show negligible bond elongation. For comparison, we investigate the energetics of nitrogen adsorption on a lithium slab, in the presence of 30 PDs that span the KT parameter space. By introducing a PD into the system, we observe new resulting nitrogen configurations with larger bond stretching. We categorize these recurring nitrogen configurations into five different states. These configurations exhibit thermodynamically favorable N_2-lithium adsorption energy over accessible states without PDs. Probing these states further, we perform a charge analysis and highlight correlations between charge transfer and nitrogen bond length. This analysis stresses the involved role of the PD in driving nitride formation.

METHODS

Computational Parameters. DFT calculations were performed using GPAW via the Atomic Simulation environment.[49,50] All structures were generated using the AutoCat software package and were relaxed until the forces on each atom fell below a convergence criterion (<0.05 eV/Å).[51] The Bayesian error estimation functional with van der Waals correlation (BEEF-vdW) was used to approximate electron−electron exchange-correlation interactions. A finite difference scheme with a target grid spacing of 0.16 Å was applied, as well as a 4 × 4 × 1 Monkhorst−Pack k-point grid for sampling the Brillouin zone of the surfaces. To improve convergence of the self-consistent field algorithm, Fermi−Dirac smearing was applied to electron occupations with a width of 0.05 eV. All adsorbates were placed on a single side of the slab, and a dipole correction was thus applied.

Nitrogen−Lithium Interactions. We first study the interactions of both nitrogen atoms (denoted as N) and N_2 molecules on the three lowest Miller index facets of lithium (100, 110, 111). For both N and N_2, all relevant symmetry sites were considered for adsorption to find the lowest energy site. For N_2, initial configurations with the molecule oriented along each Cartesian axis were investigated to enable a more extensive exploration of the potential energy landscape.

The adsorption energy between nitrogen atoms and the lithium slab is calculated using

$$E_{ads} = \left(E_{slab-nN} - E_{slab} - \frac{n}{2}E_{N_2}\right)/n \quad (5)$$

where E_{ads} is the adsorption energy, n the number of nitrogen atoms, E_{slab-X} is the DFT energy of the n nitrogen atoms (N) on the lithium slab, E_{slab} is the energy of the lithium slab alone, and E_{N_2} is the DFT energy of an isolated nitrogen molecule.

For adsorption of nitrogen molecules on the lithium slab, the analogous equation is given by

$$E_{ads} = (E_{slab-nN_2} - E_{slab} - nE_{N_2})/n \quad (6)$$

with n N_2 molecules. Here we define the DFT energy of n nitrogen molecules (N_2) on the lithium slab with $E_{slab-nN_2}$.

Nitrogen−Lithium Interactions with Proton Donor (PD) Present. To study the effects of the PD on nitrogen's interaction with lithium, nitrogen was placed between the PD and the lithium surface in our model (Figure 1). Both the PDs and the nitrogen molecule were axis-oriented, (x,y,z) meaning there were 9 combinatorial PD-nitrogen configurations. Before relaxation, the nitrogen molecule was initially placed 1.5 Å above the lithium surface. The PD was initially placed 3 Å above the lithium surface if N_2 was x or y oriented (horizontal) or 4.5 Å if N_2 was z-oriented. This increase in the z-distance was to accommodate the vertical N_2 orientation. PDs were also placed above nitrogen so that their most electrophilic atom, determined from Bader charge analysis on the molecule, was oriented above the nitrogen. Additionally, these 9 configurations were explored for the three symmetry sites (ontop, bridge, hollow) for the chosen lithium facet (100) to ensure that the energy landscape was sampled extensively. Thus, for each PD, there were 27 structural configurations. After obtaining the relaxed systems, the interaction energy between components was found using

$$E_{int} = E_{slab-PD-N_2} - E_{slab} - E_{PD} - E_{N_2} \quad (7)$$

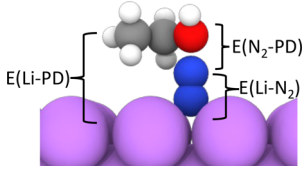

Figure 1. Schematic representation of the different energetic interactions analyzed. E(Li-PD) is the interaction energy between the lithium slab and the proton donor (PD), E(Li−N_2) is the interaction energy between the lithium slab and the nitrogen molecule, and E(N_2−PD) is the interaction energy between the nitrogen molecule and the PD.

https://doi.org/10.1021/acs.jpcc.4c08138
J. Phys. Chem. C 2025, 129, 2488−2501

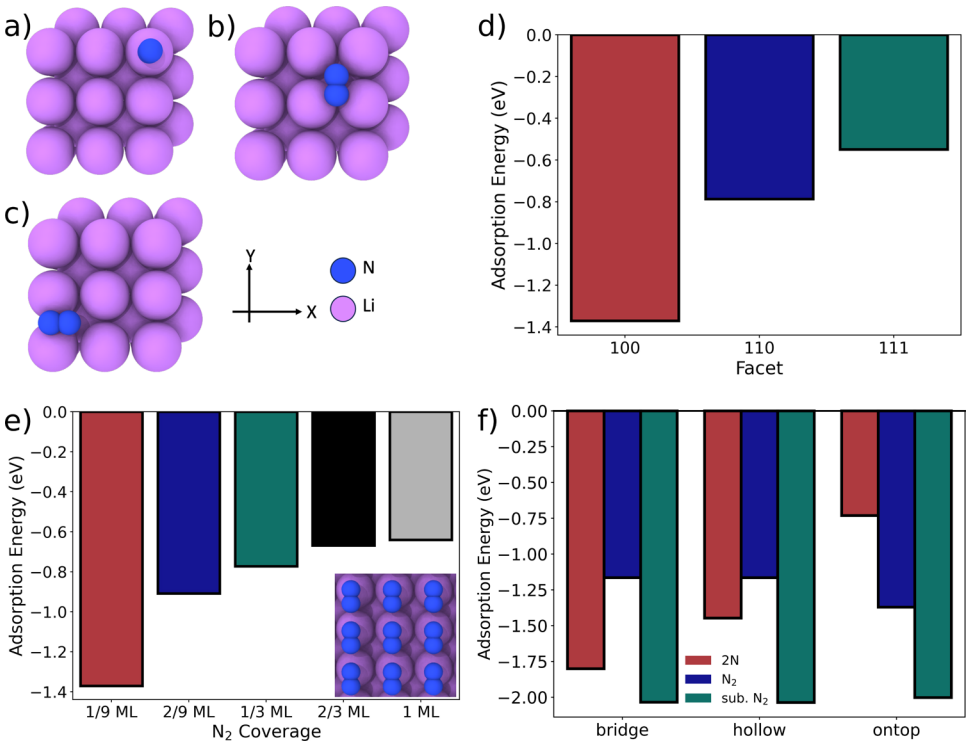

Figure 2. Initial configurations of N_2 on the lithium surface, orienting it (a) along the *z*-axis and at the ontop site, (b) along the *y* axis at the hollow site, and (c) along the *x*-axis at the bridge site. (d) Minimum adsorption energy of N_2 on the lowest Miller indice facets of lithium shows the strongest adsorption on the 100 facet. (e) Average adsorption energy of N_2 is shown to decrease as the monolayer (ML) coverage increases. Inset shows 1 ML coverage of N_2. (f) Adsorption of 2 nitrogen atoms (2N) is favored over adsorption of the nitrogen molecule (N_2) at the bridge and hollow sites but not at the ontop site. However, the formation of surface N_2 is the most favored N_2 interaction process at all sites.

where E_{int} is the interaction energy, $E_{slab-PD-N_2}$ is the DFT energy of the model system in Figure 1, E_{slab} is the energy of the lithium slab alone, and E_{PD} and E_{N_2} are the energies of the PD and the nitrogen molecule, respectively. In a system without the PD, E_{int} is the interaction energy of lithium and nitrogen and collapses to the adsorption energy. It is worth noting that the interaction energy of the surface captures the interactions between all three molecules (Figure 1). To isolate the energy of the lithium−nitrogen interaction ($E(Li-N_2)$), the PD is removed from the surface after the final configuration is obtained and the total energy is calculated for this fixed system.

Geometric Analysis and Dimensionality Reduction. Once the relaxed DFT configurations are obtained, a comparative structural analysis is performed on the final geometries. This is accomplished by removing the PDs from each relaxed configuration and then encoding the structure using DScribe's smooth overlap of atomic positions (SOAP) or SineMatrix descriptors to obtain fixed-size numeric vectors.[52−58] Here we use our group's AutoCat software as an interface to streamline this process.[51]

Once these structure encodings are obtained, dimensionality reduction is done using the Uniform Manifold Approximation and Projection (UMAP) algorithm.[59] The clusters produced by the 2-D UMAP projections are assigned group labels using the HDBSCAN clustering algorithm.[60]

RESULTS AND DISCUSSION

Nitrogen Interactions with a Lithium Surface. Our approach here to better understand the interactions present within the LiMEAS system is to decouple all of the interactions through two simplified models. Initially, we model solely nitrogen gas N_2 molecules on a lithium surface. This abstracts out all other components that are generally present in the reaction, and allows emphasis on the lithium−nitrogen interaction. By first understanding this core interaction without any external influences, we aim to provide a baseline for comparison before introducing the PD.

To start, we relaxed N_2 on the three lowest Miller index facets of lithium: 100, 110, and 111 and find the 100 and 110 surfaces to be very close in energy with the latter being more stable (Table S1).[61−64] For each of these surface facets, we enumerated adsorption at all of the unique symmetry sites: ontop (where the N_2 is directly above a surface Li atom; Figure 2a), hollow (where the N_2 lies between multiple surface Li atoms; Figure 2b) and bridge (where the anchor N_2 is 2-fold coordinated between two surface Li atoms; Figure 2c). Additionally the initial orientations of N_2 were also enumerated with respect to the Cartesian axes to enable exploration of the energy landscape (Figure 2a−c). Across all of these calculations, the most common observation was a repelling of the N_2 beyond the initial 3 Å distance from the lithium surface. However, a notable exception was when the N_2 was oriented perpendicular to the surface at the ontop site, where the N_2 adsorbed onto the lithium surface with negligible change in N_2 bond length. Even when performing similar simulations with the N_2 initially placed 1.5 Å above the slab, well within the bond-length of Li−N in lithium nitride (1.9 Å), spontaneous dissociation still was not observed in the system.[65−67] In this case, however, the N_2 was found to adsorb in all sites, whether on the surface or at the hollow site. These results imply that despite the high reactivity of lithium,

https://doi.org/10.1021/acs.jpcc.4c08138
J. Phys. Chem. C 2025, 129, 2488−2501

there remains a barrier to N_2 dissociation when considering only lithium and N_2, in agreement with previous work.[64,68]

Developing a thermodynamic understanding of N_2 adsorption on lithium, we calculate the enthalpies of adsorption on each of the surface facets using eq 6. This provides insight into the strength of the lithium-N_2 bonding without any external influences, with a more negative value indicating increased strength. Comparing the most negative adsorption energies of each considered surface facet (Figure 2d), we observe that the N_2-lithium adsorption is strongest on the 100 facet. Because lithium's role in electrochemical ammonia synthesis is presumed to primarily be a N_2 bond breaker, we focus the rest of our analysis on this facet.

Moving beyond the low-coverage limit, we next probe the impact of steric effects by varying the N_2 concentration in our calculations. We explore different coverages of the N_2 at all sites on a 3 × 3 lithium supercell, after which the minimum adsorption energy for each site is calculated using eq 6. Figure 2e shows the average adsorption energy for N_2 on the lithium slab at different coverages. We observe that as the coverage of N_2 on the surface increases, the average adsorption energy decreases. This highlights the possible role of steric effects between N_2, and may hint toward a concentration dependence of the LiMEAS reaction.

Further exploring this interaction, we next investigate dissociation through a thermodynamic lens. This is a critical step for nitride formation. While dissociation is ultimately driven by kinetics, we use the reaction energy as an initial descriptor toward understanding this process. Here, our model assumes that dissociation of N_2 would result in nitrogen atoms (2N) being placed at horizontally adjacent symmetry sites (Figure S1a). Thus, we calculated the energies for the adsorption of two nitrogen atoms (N) placed in this manner. We compared the adsorption energy minimum from this dissociated configuration to that of the nitrogen molecule at the same site. We found that N_2 has stronger adsorption on the lithium surface than two nitrogen atoms at adjacent symmetry sites for all three 100 symmetry sites (ontop, bridge, hollow) (Figure S1c). However, as shown in Figure 2f, when the nitrogen atoms were placed at diagonally adjacent symmetry sites (Figure S1b), the dissociated configuration was shown to be favored over N_2 adsorption at all sites except for the ontop site, where N_2 adsorption was favored. These results align with our observation that N_2 dissociation did not occur during geometry relaxations of the simplified model. Previous work exploring dissociation of N_2 on Li showed that N_2 dissociation usually began with the formation of some subsurface nitrogen.[64,68] We explore the energetics for the formation of this subsurface N_2 by initializing the molecule 1.5 Å into the slab and relaxing until convergence. As seen in Figure 2f, the formation of subsurface N_2 is more thermodynamically favored (−2.03 eV) over both N_2 adsorption (−1.37 eV) and the formation of surface nitride (−1.80 eV), making it the most stable Li−N_2 interaction in the 100 facet. This suggests that there is a thermodynamic drive for N_2 diffusion into bulk Li which is in contrast to results presented by Azofra et al., who predicted the preference of N_2 surface adsorption over N_2 subsurface embedding on the 100 facet with an energy difference of 0.13 eV, although this is well within the predicted uncertainty in DFT exchange-correlation functionals.[69,70] Given their prediction that surface Li_3N formation is uphill from N_2 subsurface embedding, even though bulk Li_3N formation is downhill of both processes at −3.83 eV per N_2, could suggest nitride formation may be kinetically favored over subsurface embedding on this facet.

Proton Donor (PD) Influence on N_2-Lithium Interactions. With a baseline understanding of N_2-lithium interactions, we next introduce different PDs into the model system to explicitly probe their effects on the N_2-lithium interaction strength. As in the case of modeling only lithium and N_2, we sampled the energy landscape by investigating configurations at all symmetrically unique sites. For each site, N_2 was oriented along one of the Cartesian axes, with a PD now placed above it. Similarly, PDs were also aligned along one of the three Cartesian axes, allowing for 9 N_2−PD configurations per site. Adopting this approach enables systematic investigation of how lithium-N_2 interactions differ across PDs.

Proton Donor (PD) Selection. Since PD identity will have a varying impact on lithium−nitrogen interactions, we compile a set of 30 PDs for these calculations. Driven by our previously observed correlation of KT parameters with LiMEAS activity,[46] these PDs were selected to span the KT parameter space, as shown in Figure S3. In this plot, PDs in the green quadrant was previously identified as being active toward LiMEAS.[46] Additionally, we selected borane and its fully halogenated counterparts, as BF_4 is a prominent salt component. Species with structures like THF, such as tetrahydropyran and 3-hydroxytetrahydrofuran, were selected due to being considered promising options for reducing impermeability effects of the SEI.[47] Also, aromatics like phenol and phenyl-methanol were included in our set to compare the shuttle-type PDs and the currently sacrificial PDs.[47,48] A list of all PDs considered in this work is provided in Table S4. The following subsections discuss observed trends across these PDs considered, thermodynamic implications, dissociation of final N_2 configurations, and findings from charge analysis and slab reorganization to provide fundamental insights.

Unique N_2 Configurations in the Presence of PDs. Performing geometric relaxations of our model system as described above for the selected set of PDs, we identify common themes across the final configurations. These are characterized by a combination of the N_2 bond length and orientation on the Li100 surface. Using SOAP, we encode all relaxed N_2 configurations on Li100 in the presence of each PD. As stated in the methods section, we removed the PD from the calculated slabs to focus on the N_2 configurations on Li. Additionally, to ensure consistency in analyzing the structures, any final configurations that resulted in proton transfer to the nitrogen were excluded, as this change in PD makes its removal from the surface ambiguous. Uniform Manifold Approximation and Projection (UMAP)[71] is applied to project these geometrical representations onto two dimensions, allowing them to be visualized, as seen in Figure 3.

From this projection, we observe several clusters. Looking at representative members of each group, we found that four themes are present based on how the nitrogen molecule interacts with the lithium surface. They could be grouped together by considering their nitrogen interaction strength and potential paths to dissociation (Table S3). Interestingly, we also note that the clusters are locally related by the symmetry site where the nitrogen molecule was initially placed before relaxation (Figure S2).

We name these four identified themes the (A) embedded, (B) adsorbed, (C) standing, and (D) buried states. We also define an additional state, the transferred state, to encompass

https://doi.org/10.1021/acs.jpcc.4c08138
J. Phys. Chem. C 2025, 129, 2488−2501

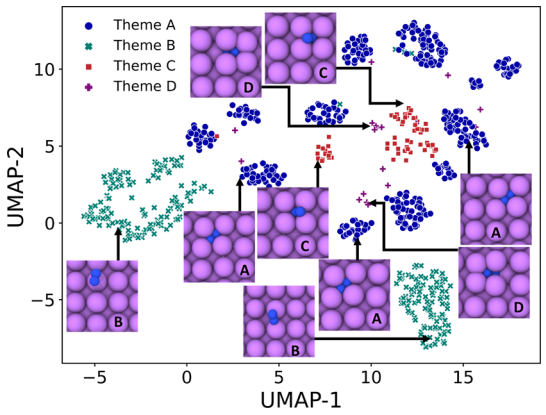

Figure 3. UMAP projection of relaxed N_2 configurations on lithium in the presence of PDs. Clusters are color-coded by emergent geometric themes with representative structures visualized as insets. Purple atoms are lithium, blue are nitrogen atoms.

all remaining states. We discuss each of these states in the following subsections and visualize representative structures Figure 4a–e.

Embedded State. Of these 4 themes from geometric analysis, the most commonly observed is the embedded state (Figure 4a). It is characterized by a final configuration in which the nitrogen molecule adsorbs horizontally within the first layer of the slab, lodging itself between two surface lithium atoms that are diagonal from each other. Generally, this state yielded an average nitrogen bond length change of 14.8%. We note that this state bears similarities to previously reported structures of N_2 on Li and Ca.[64,68,72]

Adsorbed State. The second most frequently observed state is the adsorbed state. Here the nitrogen molecule rests above the surface and has only one of its nitrogen atoms interacting with the surface (Figure 4b). Most adsorbed state configurations have bond length changes below 5% with the average change in bond length being 3.2%.

Standing State. We additionally define the standing state as any configuration for which one of the nitrogen atoms in the N_2 adsorbs onto a lithium atom in the subsurface layer of the slab, at the hollow site. In general, the other nitrogen atom of the molecule interacts with one or more lithium atoms on the surface (Figure 4c). This state showed a relatively high variability in N_2 bond length, ranging from 12 to 20%, though the mean bond length change was 14.4%.

Buried State. The buried state, which usually occurs at bridge sites, is characterized by the whole nitrogen molecule fully entering the subsurface of the lithium slab (Figure 4d). The buried state was characterized by the highest bond length changes with an average of 19.8%.

Transferred State. These first four states represent those in which the nitrogen molecule remained unbonded to PD atoms in their final configuration. In addition to these, there was a fifth group, created as a catchall for all final configurations which resulted in the transfer of protons to the nitrogen, or within which some form of PD decomposition occurred

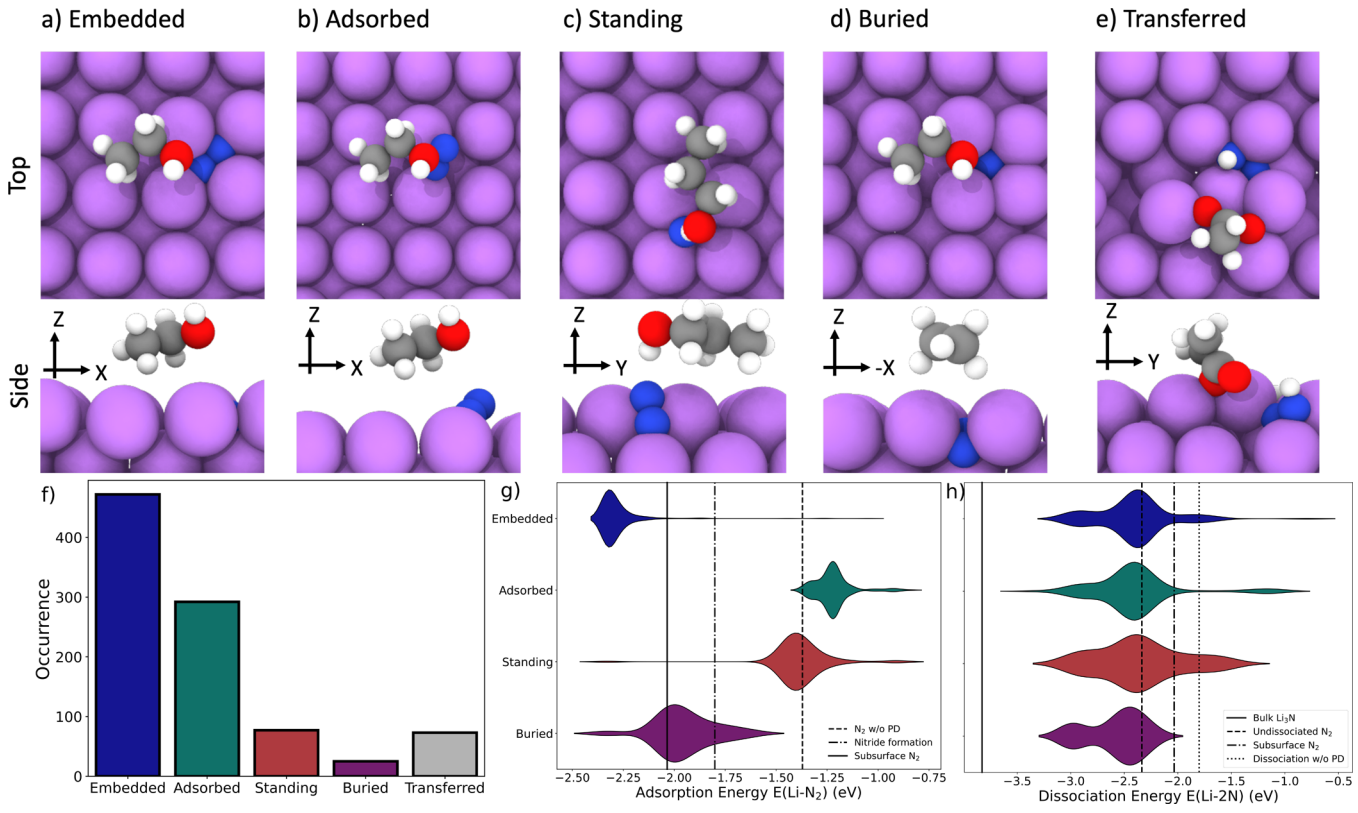

Figure 4. (a–e) Example structures of the emergent recurring nitrogen configuration states in the presence of a PD. (f) Histogram of the number of times each nitrogen state emerged from the presence of a PD across all relaxations performed in this study. (g) Violin plot of N_2 adsorption energies on Li categorized by PD-encouraged states. The nitrogen adsorption energy of the relaxed configuration in the absence of a PD and nitride formation energies are provided as vertical dashed lines for reference. (h) Violin plot of 2N dissociation energies of the different states on Li. References for competitive N_2 process like PD-N_2 adsorption, subsurface N_2 formation and dissociation without PD are provided.

https://doi.org/10.1021/acs.jpcc.4c08138
J. Phys. Chem. C 2025, 129, 2488–2501

(Figure 4e). As the focus of this study is primarily on the PD effect on the N_2-lithium interaction in its unprotonated states, these decomposed and altered states, collectively referred to as the transferred states, are not included in the rest of this analysis.

In the presence of the PD, the first four described states (embedded, adsorbed, standing, and buried) denote four ways N_2 interacts with the lithium slab. In the absence of the PD however, only the adsorbed and standing states were observed, implying that the presence of the PD results in new N_2-lithium configurations. The distribution of states in the presence of the PD shows that the newly emergent embedded state was by far the most prevalent (Figure 4f). The adsorbed and standing states follow in order of prevalence with the buried state, an emergent state similar to the observed subsurface N_2, rounding them off. The appearance of the embedded and buried states only in the presence of the PD suggests that it is not just a spectator and may have an additional role in inducing unique N_2-lithium interactions.

Thermodynamics of PD-Influenced Nitrogen Configurations. Having identified these recurrent nitrogen states, we now probe the thermodynamics of the various interactions within the PD-lithium−nitrogen system. In conducting this analysis, we note the interaction energy from eq 7 comprises the total interaction of all components in the system, including pairwise and three-way interactions. As shown in Figure 1a, the interactions in our system can be broken down into the pairwise interactions between components. Here, our focus is on the strength of the N_2-lithium interaction, characterized by the adsorption energy ($E(\mathrm{Li{-}N_2})$). To extract this quantity, we removed the PD from the final system and extracted the potential energy of the PD-absent structure. Eliminating the PD's interaction with nitrogen and lithium allows us to control for variance in the final PD configuration and enables a more representative comparison of energies within and between the nitrogen states.

To understand the thermodynamics of these configurations, we plot the distribution of adsorption energies of these final states in Figure 4g. These energies are contextualized against the most thermodynamically favorable adsorption configuration accessible by nitrogen without the presence of a PD. This baseline is represented by the vertical dashed line in this plot. Contextualizing in this manner allows us to compare the thermodynamic favorability of the accessible states in the presence and absence of the PD.

In Figure 4g, we see that the two states that only appear in the presence of the PD, namely the embedded and buried states, are more energetically stable than the states that also exist in the absence of the PD (the adsorbed and standing states). More importantly, these new states mainly fall to the left of the line showing the most stable N_2-lithium interaction in the absence of the PD and also the most stable energy for forming surface nitrides (see Figure 2f). This suggests that the newly emerging states, embedded and buried, are generally associated with stronger N_2-lithium interactions. The similarity between the buried state occurring in the presence of the PD and the subsurface N_2 configurations occurring in their absence suggests that some PDs are able to interact with N_2 in ways that allow it to overcome the barriers to subsurface embedding. Additionally, that most embedded states are to the left of the line representing the most thermodynamically stable subsurface N_2 state suggests an inhibitive PD influence against diffusion into the bulk. Since the embedded state is the most commonly observed state in the presence of the PD, this suggests that the PD can facilitate the formation of states with stronger surface lithium−nitrogen interactions. This finding has implications for nitride formation as it showcases the PD as more than a spectator for this process.

Dissociation of PD-Influenced Nitrogen Configurations. We explore the pliability of these states to dissociation by perturbing the distal nitrogen atom into the nearest neighbor symmetry site, keeping the PD on the Li surface to maintain its influence on the $\mathrm{Li{-}N_2}$ interaction. We adopt the same process as with quantifying the PD influence on N_2 adsorption, obtaining a final configuration post-relaxation, extracting the potential energy of the PD-free slab, and then using eq 5 to calculate the adsorption energy of the dissociated N_2 on the surface. In Figure 4h, we show the distribution of calculated dissociation energies of each state, contextualizing them with the energy of the dissociated state in the absence of the PD, the energy of the most thermodynamically favored embedded state, and the most thermodynamically favored subsurface N_2.

Figure 4h shows that all states, whether embedded, adsorbed, standing or buried, have majority of their dissociation energies fall much to the left of the energy of the most thermodynamically favored PD-induced/embedded state. This immediately suggests that there is a thermodynamic drive and thus a viable pathway to Li_3N formation for all states, even the embedded and buried states, which are characterized by higher $\mathrm{Li{-}N_2}$ interactions. That they fall to the left of the subsurface N_2 line suggests that diffusion into the bulk would be less favored than dissociation in the presence of the PD, implying that, ignoring kinetic barriers, bulk diffusion is not inhibitive to nitride formation from 2 nitrogen atoms. Perhaps most surprisingly, the most dissociative states fall far to the left of the line representing dissociation in the absence of the PD. This confirms an additional role the PD could play in nitride formation, as its induced undissociated N_2 states show pathways to more energetically stable Li_3N. We would like to highlight that though Li_3N forms favorably in the presence of the PD, the activation barriers toward dissociation may be dependent on both the PD and the state. Given the complexity of the energy landscape, however, this will be investigated in a future study.

Understanding the Recurring N_2 States via Charge Analysis. To better understand these new nitrogen configurations we perform a Bader charge analysis[73] to calculate the charge distribution around the nitrogen atoms. Previously, this method has been used to understand the electrolyte role in SEI formation in lithium metal batteries.[36] This allows us to understand the magnitude of the charge transfer onto the different nitrogen states. Moreover, our analysis considers separately the charge transferred to the electrophilic and nucleophilic nitrogen atoms comprising N_2. First, the embedded state gained a total average charge of −2.23 with the average charge on the nucleophilic nitrogen being −1.13 and that on the electrophilic nitrogen being −1.09. In comparison, the buried state had the largest average charge gain of −2.78. Breaking this charge gain down by atom, nucleophilic and electrophilic atoms share this charge with values of −1.46 and −1.32, respectively. For the standing state, the total charge gained for the N_2 was much closer to that of the embedded state at an average of −2.13, with a much greater difference in the nucleophilic/electrophilic split. The nucleophilic nitrogen on average gained a charge of −1.43 whereas the electrophilic nitrogen atom gained a charge of

https://doi.org/10.1021/acs.jpcc.4c08138
J. Phys. Chem. C 2025, 129, 2488−2501

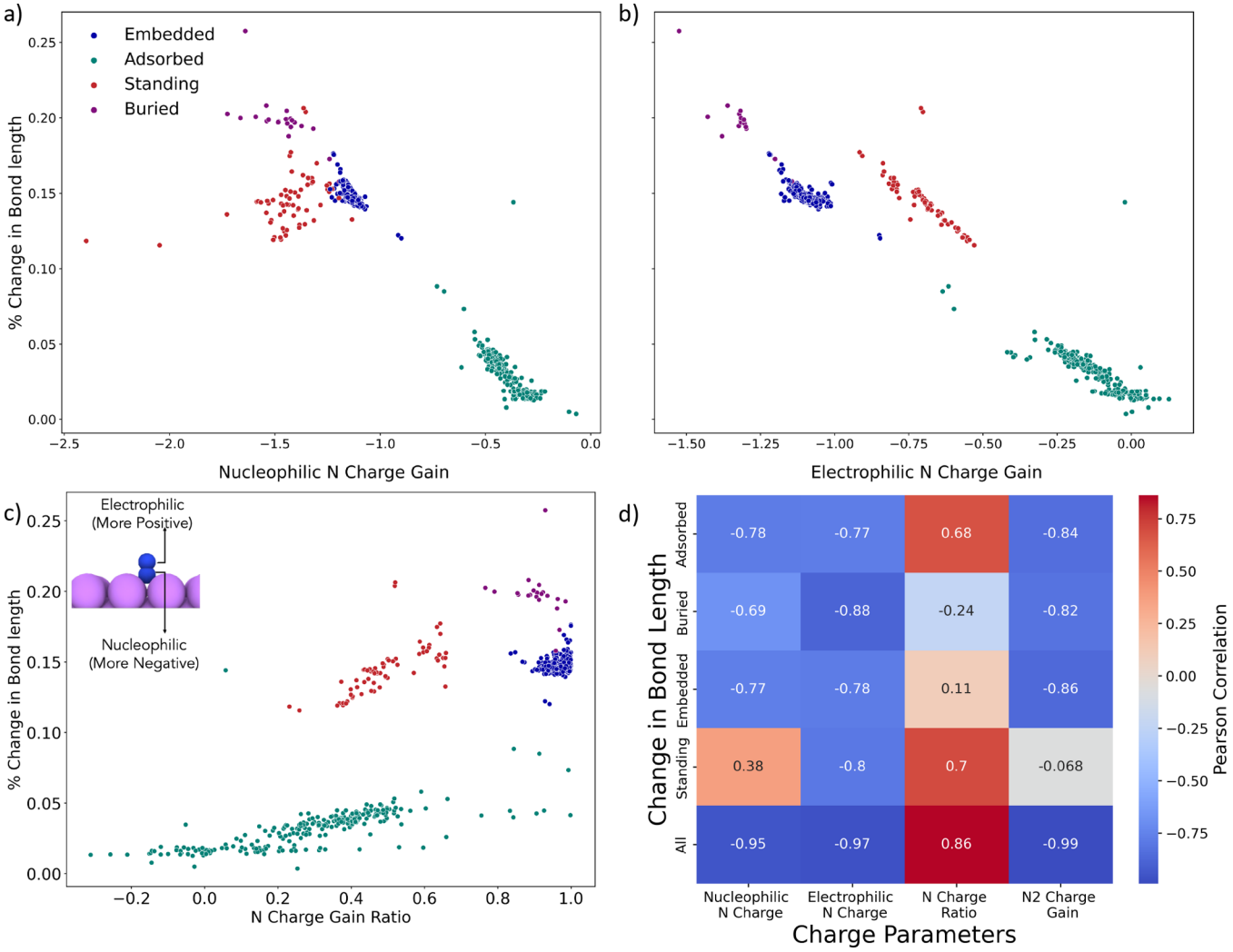

Figure 5. Bader analysis plots of comparing the change in nitrogen molecule bond length to (a) charge gained on the more negative (nucleophilic) nitrogen atom, (b) charge gained on the more positive nitrogen (electrophilic) atom, and. (c) ratio of charged gained on both nitrogen atoms. (d) Pearson correlation heatmap of the correlation between the change in bond length with the charge characteristics of the nitrogen states.

−0.70. Lastly, the adsorbed state is found to have the smallest overall charge gain around −0.54 with a charge split of −0.41 on the nucleophilic nitrogen atom and −0.13 on the electrophilic nitrogen atom. In short, the differences in charge transfer across these states highlight the distinct character between the recurring states.

Further analyzing the properties of these states, we probe the connection between charge transfer and bond length. Since charge transfer onto the nitrogen corresponds to the transfer of electrons into the antibonding orbitals of the nitrogen molecule, we can expect that charge gained to correlate with an increase in N_2 bond length. We thus compare the charge gain characteristics of these nitrogen states to the bond length change as we are interested in the pliability of these states toward lithium-assisted N_2 dissociation.

We first consider the charge gained on each of the nitrogen atoms in N_2 as a function of the change in bond length. In Figure 5a, we plot the charge gained on the most negative (nucleophilic) nitrogen atom with respect to the bond change in the nitrogen bond length. We see that for the adsorbed, embedded, and buried state, as the nitrogen atom becomes more negative, there is a corresponding increase in the bond length. For the standing state, the bond length increases as the charge on the negative nitrogen atom decreases. Considering the charge on the more positive (electrophilic) nitrogen atom, we find for all states that as the charge on the nitrogen atom becomes more negative, the bond length increases. Because the nitrogen starts neutrally charged, the additional negative charge suggests the transfer of electrons onto the nitrogen molecule. Thus, the bond length increases with charge gained, as expected. We additionally note that the states only observed in the presence of a PD (embedded and buried) have both higher magnitudes of the charge transferred onto the single nitrogen atoms and the change in bond lengths. As a result, these states may be more reactive and determine the initial stages of nitride formation.

Next, we further investigate the prospects for increased reactivity of the nitrogen molecules. Because the nitrogen molecule is naturally neutral, the charge differential created by the electron transfer from the lithium slab to the nitrogen states could affect reactivity toward protons or other nearby lithium atoms. Thus, we calculate the ratio of the charge of the electrophilic nitrogen to the nucleophilic. This allows for gauging the possible reactivity of the nucleophilic nitrogen atom with an electrophilic proton in the case of associative nitrogen protonation. We find that the most thermodynami-

https://doi.org/10.1021/acs.jpcc.4c08138
J. Phys. Chem. C 2025, 129, 2488−2501

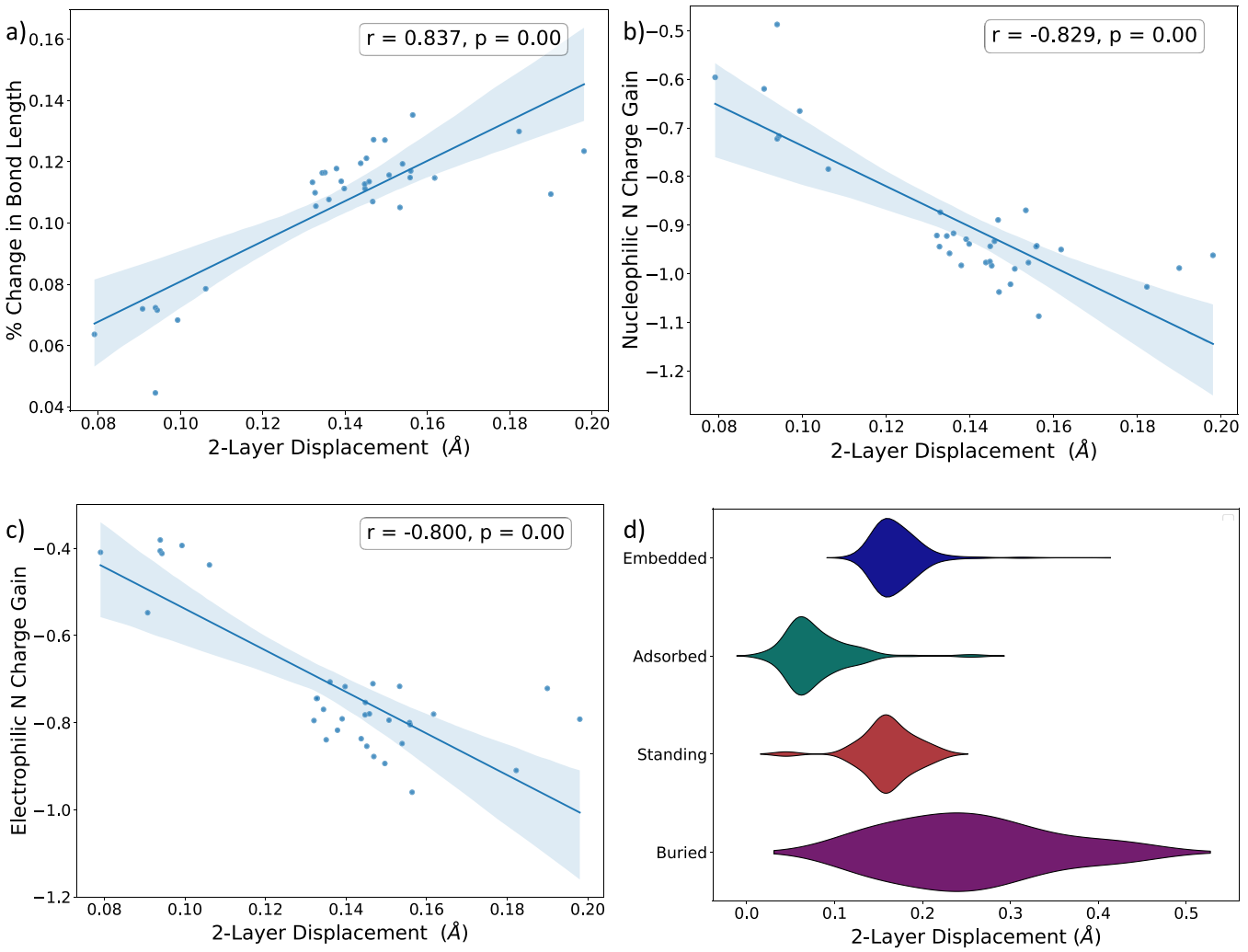

Figure 6. Correlations between the median 2-layer displacement of each PD and (a) the median change in N_2 bond length. (b) Median charge gained on the nucleophilic nitrogen atom, and (c) the median charge gained on the electrophilic nitrogen atom. (d) Violin plot showing the distribution of the 2-layer displacement across the nitrogen states.

cally stable embedded state has an average charge ratio of 0.97, with both nitrogen atoms gaining nearly the same charge. This is followed by the buried state with a charge ratio of 0.90, the standing state with a charge ratio of 0.50, and the adsorbed state with an average charge ratio of 0.30. We observe that the states with a charge ratio closer to unity are associated with stronger N_2-lithium interactions and have more stable adsorption energies than the states with lower charge ratios. To emphasize this point, Pearson correlation analysis shows that the adsorption energy ($E(Li{-}N_2)$) has a strong negative correlation with the charge ratio at −0.84.

Based on the charge ratios and the total magnitude of charge gained, we would expect that in an associative type protonation reaction, the nitrogen atoms of the embedded state would be similarly reactive toward an electrophilic proton because of their comparable charges. Likewise, we would expect roughly equal reactivity of the nitrogen atoms for the buried state though its orientation makes one nitrogen more available to protons than the other. The standing state would theoretically be most reactive toward an electrophilic proton because of the large negative charge on its nucleophilic nitrogen. However, its orientation is such that this nitrogen atom is more proximal to the lithium and thus is less available for protonation than its distal electrophilic nitrogen atom. The adsorbed state, which was the second most abundant state, in principle has both nitrogen atoms accessible for protonation, though its low magnitude in charge ratio likely leaves its reactivity to protons lacking.

Figure 5c shows our investigation into the possible dependence of the change in bond length on the charge ratio. For the adsorbed state, which had the lowest magnitude of charge gained and the lowest ratio of charges, we observe a roughly linear increase in the bond length change with the ratio of charges on the nitrogen molecule (Pearson correlation of 0.68). A similar phenomenon is observed in the standing state which has both a higher average charge on the nitrogen molecule and ratio of charge between its nitrogen atoms. For the more stable buried state, we observe a weak negative correlation between the bond length changes and the charge ratio on the nitrogen atoms and for the embedded state (Pearson correlation of 0.11). Thus, for these states the bond length changes are largely independent of the ratio. Further investigations of these states are required to concretize any correlations between these two parameters.

To draw further insights from our correlation analysis, we calculate the correlation between the individual states and the

https://doi.org/10.1021/acs.jpcc.4c08138
J. Phys. Chem. C 2025, 129, 2488−2501

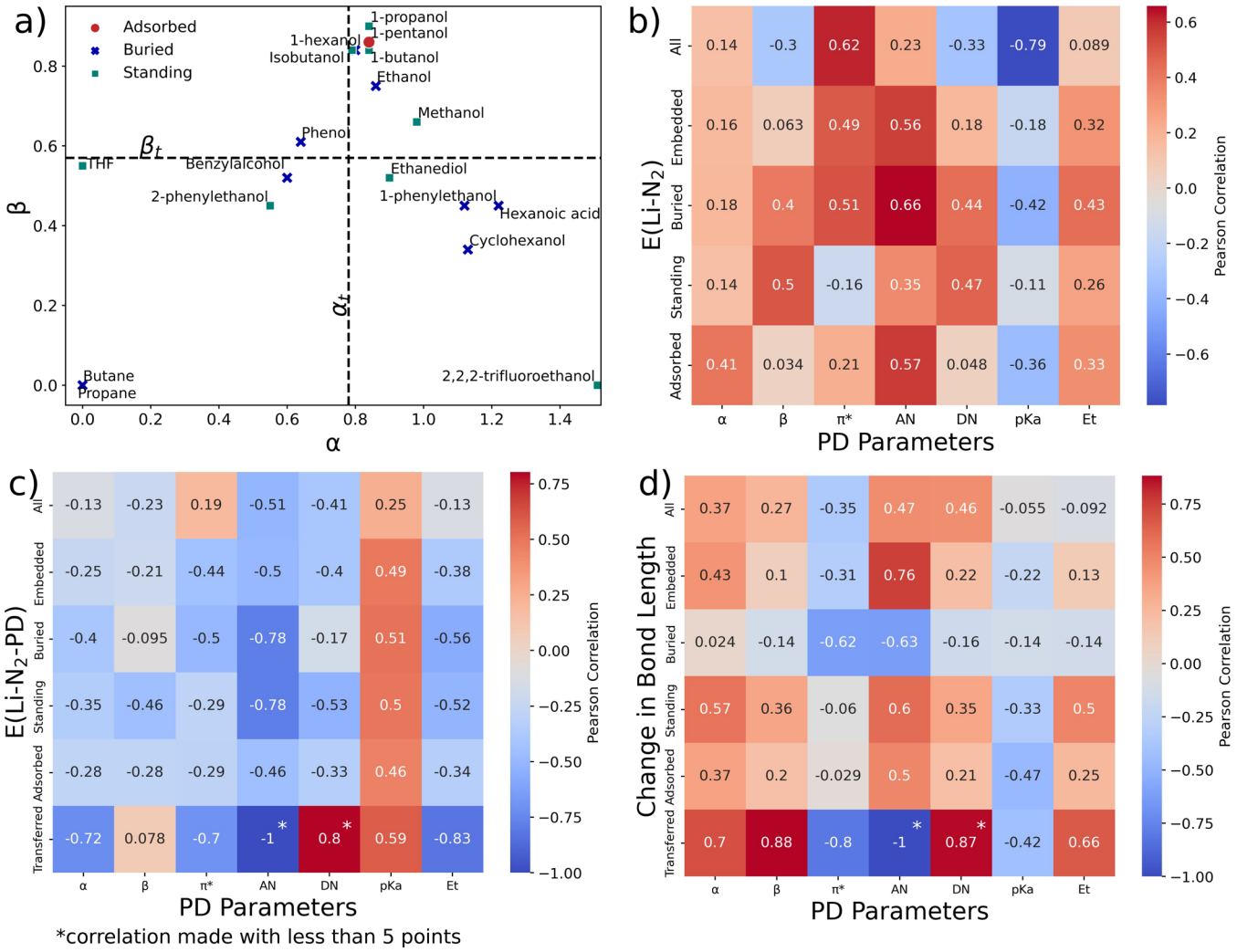

Figure 7. (a) Mapping of Kamlet Taft (KT) parameters of all PDs to their *second* most favorable state. (b–d) Pearson Correlation heatmaps showing the correlation of (b) change in bond length, (c) the interaction energy E(Li–N_2-PD), and (d) the nitrogen adsorption energy E(Li–N_2) of the unique states with physicochemical properties of the PD species.

various charge parameters (Figure 5d). In addition, we also examine the correlation using the change in bond length across all states (labeled as *All*). When comparing the charge gained on the nucleophilic nitrogen to the change in bond length, we observe that all states but the standing state show a strong negative correlation, with the correlation across all states being −0.95. A similarly strong correlation is seen across and within all individual states between the charge gained on the electrophilic nitrogen and the change in the bond length, with a correlation of −0.97 across all states. Between the charge ratio of the nitrogen atoms and the bond length, we find a strong positive correlation of 0.86, though the buried and embedded states show weak or no correlation between these two parameters. Finally, for the total charge gained, all individual states show a strong negative correlation with the change in bond length, except the standing state within which the change in bond length largely remains independent of the total charge on the molecule. The combined correlation across all states, however, is strong at −0.99. These results suggest that PDs that facilitate more charge transfer onto the nitrogen molecule generally result in larger bond length changes, essential for nitrogen dissociation.

Mechanism of PD Influence on the N_2 States. We seek to understand the source of the PD's influence on stabilizing Li–N_2 interactions. Building on the numerous structures enumerated earlier, we propose that the presence of PD might be causing a rearrangement of lithium atoms to promote the formation of more stable nitrides. To examine this possibility, we assess slab reorganization by measuring the average positional displacement of atoms in the two freely moving layers of the final configuration relative to a reference slab. This 2-layer displacement serves as an indicator of reorganization and is calculated using

$$2-\text{layer displacement} = \frac{1}{N}\sum_{i=1}^{N}\sqrt{(x_i-x_0)^2+(y_i-y_0)^2+(z_i-z_0)^2} \quad (8)$$

where $(x, y, z)_i$ represent atomic positions in our final configuration and $(x, y, z)_0$ represent atomic positions in our reference slab. For each slab, we use as our reference the corresponding PD-free N_2 final configuration in order to provide an estimate of how the PD increases rearrangement of the Li atoms relative to the baseline.

https://doi.org/10.1021/acs.jpcc.4c08138
J. Phys. Chem. C 2025, 129, 2488–2501

In Figure 6, we look at how the summary statistics of various final configuration characteristics vary with the 2-layer displacement using the median as our preferred summary statistic to reduce the impact of outliers on our analyses. For each characteristic, we consider the correlation with the 2-layer displacement and assume a significance level of 0.05 for all statistical tests. We define any correlations to be nonexistent if between 0 and 0.3, weak between 0.3 and 0.5, moderate from 0.5 to 0.7, strong from 0.7 to 0.9, and near perfect if above 0.9.

Circling back to Li's main role as a N_2 bond breaker, we compare the median 2-layer displacement to the median change in N_2 bond length for a given PD (Figure 6a). We find a strong positive correlation (0.837) between the bond elongation of the N_2 and the 2-layer displacement, suggesting that increased Li slab rearrangement is associated with greater N_2 bond weakening. Across our entire data set (Figure S4a), this correlation still holds, being slightly weaker at 0.757. The 2-layer displacement is also shown to have strong negative correlations with the charge gained on the nucleophilic N atom (−0.829—Figure 6b) and a similarly strong negative correlation with the electrophilic nitrogen charge (−0.800—Figure 6c). From this we find that an increase in the reorganization of the slab is associated with an increase in charge transfer to the N_2 molecule, suggesting that the presence of PD enables Li surface movement, allowing N_2 to take configurations with increased charge transfer. This idea is corroborated by Figure 6d which shows the distribution of the 2-layer displacement across the N_2 configurations. Here, we find the adsorbed state, which we know from Figure 5 and Table S10 to be associated with the lowest magnitude of charge transfer, is shown to be associated with the lowest 2-layer displacement. The standing and embedded states are shown to have higher 2-layer displacements with means at 0.18 Å and 0.2 Å. The buried state is shown to have the greatest mean 2-layer displacement at 0.25 Å. From Table S10, we see that majority of the charge gained by N_2 originates from the metal, and not the PD, with the PD gaining the least charge of all three components in our system. This, in conjunction with the observed increase in Li slab reorganization, highlights the mainly facilitative role of the PD. In the next section, we delve deeper into how the PD's chemistry affects the evolved characteristics of these states.

Evaluating Kamlet−Taft Parameters as N_2 Configuration Predictors. Going back to our defined N_2 configuration states, we next evaluate the ability of KT parameters to predict their formation from solely the PD. As mentioned earlier, we have previously shown that these parameters are descriptors for overall LiMEAS activity which motivates this analysis.[46] Mapping these parameters to each PD (Figure S5), we observe that the most energetically favorable state is the embedded state across KT parameter space. In Figure 7a when considering the next most stable state, we find that different states appear for different PDs. This suggests that while PD identity may be linked to the evolution of these states, the Kamlet−Taft parameters are insufficient to fully describe the formation of the N_2 configurations. As the Kamlet−Taft α and β are descriptors of hydrogen bond donation and accepting ability,[74−76] this is expected in states where proton transfer does not occur. In other words, we would expect a Kamlet−Tafts correlation to be associated with hydrogenation/proton transfer steps in the lithium-mediated ammonia synthesis. As we have considered primarily the nitrogen molecule interaction in this paper, a Kamlet−Taft correlation here would indicate a proton-coupled nitrogen adsorption step (N_2+H* → NNH*), the first step of the associative pathway.

To explore this idea, we performed additional analyses, investigating the correlations between the interaction energies E(Li−N_2-PD), nitrogen adsorption energies E(Li−N_2), and the change in bond length of the nitrogen molecule with the Kamlet−Taft parameters. To probe the possible effects of molecular polarity on state formation and properties, we include in our analysis the Kamlet−Taft π^* parameter.[77] We also expand our parameter list to include other measures of acidity (Gutmann acceptor number (AN),[78,79] the acid dissociation constant (pK_a), and the Dimroth and Reichardt E_T[80,81]) and basicity (Gutmann Donor number[78,79]). Our analysis uses the median as our preferred summary statistic for correlations to reduce the impact of outliers. Similar to the previous section, we classify correlation values of magnitude from 0 to 0.3 to be a negligible correlation, between 0.3 and 0.5 to be a low correlation, between 0.5 and 0.7 to be moderate, between 0.7 and 0.9 to be strong, and above 0.9 to be nearly perfect.

We first consider the correlation of the PD properties with the nitrogen adsorption energy on Li, E(Li−N_2) (Figure 7b). We observe that the Kamlet−Taft π^* parameter and the pK_a of the PDs show a moderate correlation with the strength of the nitrogen−lithium interaction. The acid dissociation constant (pK_a) which is an indicator of electron-pair accepting activity for Lewis acids shows a negative correlation of −0.6 with the nitrogen−lithium interaction strength. This implies increasing pK_a (and thus decreasing acidity) of the PD increases the adsorption strength of nitrogen on lithium.

To rationalize this negative pK_a correlation with E(Li−N_2), we consider the fundamental chemistry underlying the lithium-catalyzed nitrogen reduction reaction. To facilitate lithium-mediated reduction of nitrogen via its dissociation through nitride formation, lithium must act as a reducing agent to convert nitrogen to its nitride by donating electrons to it[19−23] (see eq 2). While the nitrogen molecule is in itself very stable owing to its triple bond,[82] a strong enough Lewis acid can engage in an electrophilic attack on the nitrogen molecule's terminal lone pairs to make its atoms electron deficient enough, allowing the electron transfer from the lithium slab. This is similar to acid-catalyzed hydrolysis of nitriles (R-C≡N:) to carboxylic acids[83−87] or the reaction of nitriles with organolithium, organo-magnesium or organo-aluminum reagents to form aldehydes.[88−92] Along these lines, a stronger acid would naturally result in a weaker interaction with the lithium slab by attempting to pull more electrons away from the nitrogen atoms. In support of this rationale, we find that across all calculations, Bader analysis showed a positive charge gain on the lithium slab mostly accompanied by a negative charge gain on the PD, with the notable exceptions being molecules like propane and ethane that are poor electrophiles and have the highest pK_a (Table S10), implying electron loss mainly from the Li slab.

Continuing our investigation into PD parameter correlation with the nitrogen−lithium adsorption energy, the Kamlet−Taft π^* (polarity) parameter on the other hand shows a moderate positive correlation (0.58) across all the states in Figure 7a. Being a measure of the polarity of the molecule,[77,93] this suggests that PDs that are more polar result in less favorable nitrogen−lithium interactions. This observation aligns with our earlier hypothesis of an electrophilic attack on the nitrogen

https://doi.org/10.1021/acs.jpcc.4c08138
J. Phys. Chem. C 2025, 129, 2488−2501

molecule to make it more electron deficient. Since highly polar molecules will possess more prominent electrophilic centers, we anticipate electrons would be pulled away from the nitrogen molecule to allow reduction by the lithium slab in this scenario. Indeed, as the Bader analysis in the previous section shows, nitrogen interaction in the embedded, buried, and standing states is accompanied by electron transfer onto one or both nitrogen atoms (Figure 5). Thus, it is reasonable that PDs with stronger electron-withdrawing centers more easily facilitate this electron transfer.

Looking deeper at the state-wise breakdown, we find that π^* shows a strong positive correlation (0.7) for the buried state, and a moderately positive correlation (0.5) for the embedded state, which is relevant as these are the states with the highest total charge transfers onto the nitrogen molecule (Figure 5 and Table S1). The Gutmann Acceptor number, another measure of Lewis acidity strength shows a moderately positive correlation with the nitrogen−lithium interaction energy in line with already established arguments for both the buried (0.66) and embedded states (0.56). That it shows a similarly moderate positive correlation (0.57) with the interaction strength of the adsorbed state means that strong Lewis acids generally affect the adsorption strength of the nitrogen molecule. The difference in correlation behavior with the Kamlet π^* parameter may hint at the possibility of using different PD parameters to select for certain states.

Turning to PD correlations with the three-way interaction energy E(Li−N_2-PD), polarity and acceptor number also appear to be moderately correlated (Figure 7c). While we have focused on the nitrogen−lithium adsorption energy E(Li−N_2) so far as it quantifies how much more the PD stabilizes the interaction, this energy quantifies the stability of the overall system. Thus, the negative correlation seen across all states suggests increasing polarity and Lewis acidity of the PD decreases the energy of the threeway interaction, thus making the overall system more stable. As expected, this results in moderately positive correlating pK_a values for all our states ranging from 0.42 to 0.55. These results taken with the correlations for E(Li−N_2) suggest that while strong Lewis acids and electrophiles weaken the nitrogen−lithium interaction by withdrawing electrons from the nitrogen molecule, the PD stabilizes the overall interaction. This explains why the embedded and buried were not seen in the absence of the PD.

For the transferred state in Figure 7c, the three-way interaction energy E(Li−N_2-PD) shows a strong negative correlation with the Kamlet−Taft α parameter (−0.72). As α is a measure of the hydrogen bond acidity, this implies increasing bond acidity of the PD results in more negative interaction energies and a stabler protonated system. Furthermore, the Dimroth and Reichardt E_T, another measure of Lewis acidity, also shows a strong negative correlation with the interaction energy (−0.83) whereas the pK_a shows a moderately positive correlation (0.55). We do not consider the high correlations from the Gutmann acceptor and donor numbers here because they are made with fewer than 5 points, and thus cannot be considered statistically significant.

Next, we evaluate the correlation of PD parameters with the change in bond length in Figure 7d. We observe that increasing Lewis acidity (AN) of our PD generally leads to an increase in the N_2 bond length for the embedded, standing, and adsorbed states showing moderate to strong correlations of 0.76, 0.6, and 0.5, respectively. This is consistent with expectations for elongation due to strong electrophilic interactions. Perhaps surprisingly, the buried state shows a moderate negative correlation with Lewis acidity (AN) (−0.63) and polarity (−0.55) of the PD, suggesting higher acidity leads to shorter bond lengths. The difference in behavior with the other three states may be gleaned from the difference in their structure. As can be seen in Figure 4a−e, the buried state is the only state with a final subsurface nitrogen configuration which may affect how it interacts with the PD and the lithium slab when compared to the other surface configurations.

In line with our expectations, the transferred state in Figure 7d shows a strong positive correlation (0.7) with the KT α parameter, suggesting that increasing hydrogen-bond donation ability of the PD results in higher changes in the bond length of the protonated nitrogen molecule. The other measures of acidity, primarily the Kamlet π^* and the Dimroth-Reichardt E_T also show similarly positive correlations with the bond length change. The strongest correlating parameter to the change in bond length is, however, the KT β parameter, showing a strong positive correlation at 0.88, suggesting that the final nitrogen bond length increases with increasing ability of PD to accept hydrogen bonds. This is again consistent with findings by Krishnamurthy et al.[46] which suggests that the high α and β PDs were more favorable to high current efficiencies in lithium-mediated nitrogen reduction. Our findings thus suggest that amphiprotic PDs, capable of both accepting and donating protons, are more conducive to larger bond lengths for a protonated nitrogen molecule. Thus, for PD assisted nitrogen dissociation, Figure 7d suggests that stronger acids result in longer bond lengths for nonprotonated states, whereas for protonated states, amphiprotic PDs of both high hydrogen-bond donation and accepting ability correlate with longer nitrogen bond lengths.

As a final note, both the interaction energy and change in bond length in the transferred state where a proton is transferred from the PD to form NNH show strong correlations ($\geq$|0.7|) with the Kamlet−Taft α (Figure 7c,d). This supports our earlier assertion that the Kamlet−Taft parameters would be significant for predicting protonation. Thus, for a purely dissociative pathway, the Kamlet−Taft α and β parameters may be more appropriate for the subsequent hydrogenation steps beyond the scope of this study.

CONCLUSIONS

In this work we explored the effects of 30 proton donor (PD) species on the nitrogen adsorption on lithium using DFT. We show that the presence of PD species during nitrogen adsorption results in four unique and recurrent nitrogen configurations on the lithium surface: embedded, adsorbed, buried and standing. Of these recurring states, the embedded and buried states were found to have adsorption energies much greater than nitrogen's adsorption energy on the lithium surface in the absence of the PD. Additionally, these energetically favorable states were found to have significantly larger bond length changes (on average 15% for the embedded state and 20% for the buried state) compared to when nitrogen interacted with lithium in the absence of the PD. Through charge analysis, we found that the magnitude of charge transfer to the nitrogen molecule correlated directly to the extent of this bond elongation. And finally, though we observe that the Kamlet−Taft parameters were insufficient to fully describe the formation of nonprotonated states, we found that the characteristics of individual states show strong correlations with PD chemistry, and that the Kamlet−Tafts parameters are

https://doi.org/10.1021/acs.jpcc.4c08138
J. Phys. Chem. C 2025, 129, 2488−2501

correlating parameters only for the protonated (transferred) state. This work highlights the nonspectator role of the PD in nitride formation for LiMEAS and presents an additional design parameter to consider in our progress toward sustainable ammonia synthesis.

■ ASSOCIATED CONTENT

Supporting Information

The Supporting Information is available free of charge at https://pubs.acs.org/doi/10.1021/acs.jpcc.4c08138.

Additional discussion on thermodynamics details, dimensionality reduction and clustering, statistics of observed states, and details of chemical species used (PDF)

■ AUTHOR INFORMATION

Corresponding Author

Venkatasubramanian Viswanathan − *Department of Mechanical Engineering, Carnegie Mellon University, Pittsburgh, Pennsylvania 15213, United States; Department of Chemical Engineering, Department of Mechanical Engineering, and Department of Aerospace Engineering, University of Michigan, Ann Arbor, Michigan 48109, United States;* orcid.org/0000-0003-1060-5495; Email: venkvis@umich.edu

Authors

Victor Azumah − *Department of Mechanical Engineering, Carnegie Mellon University, Pittsburgh, Pennsylvania 15213, United States; Department of Chemical Engineering, University of Michigan, Ann Arbor, Michigan 48109, United States*

Lance Kavalsky − *Department of Mechanical Engineering, Carnegie Mellon University, Pittsburgh, Pennsylvania 15213, United States; Department of Mechanical Engineering, University of Michigan, Ann Arbor, Michigan 48109, United States;* orcid.org/0000-0002-7875-5652

Complete contact information is available at: https://pubs.acs.org/10.1021/acs.jpcc.4c08138

Notes

The authors declare the following competing financial interest(s): V.V. is an inventor on a provisional patent application, 63/066841, related to hydrogen donors for lithium-mediated ammonia synthesis.

■ ACKNOWLEDGMENTS

L.K. acknowledges the support of the Natural Sciences and Engineering Research Council of Canada (NSERC).

■ REFERENCES

(1) Rouwenhorst, K. H. R.; Van der Ham, A.; Mul, G.; Kersten, S. *Power-to-ammonia-to-power (P2A2P) for local electricity storage in 2025*. In Current Developments, Process Proposal & Future Research Required. University of Twente, 2018, 8.

(2) Erisman, J. W.; Sutton, M. A.; Galloway, J.; Klimont, Z.; Winiwarter, W. How a century of ammonia synthesis changed the world. *Nature geoscience* **2008**, *1*, 636−639.

(3) Nørskov, J.; Chen, J.; Miranda, R.; Fitzsimmons, T.; Stack, R.; *Sustainable Ammonia Synthesis—Exploring the Scientific Challenges Associated with Discovering Alternative, Sustainable Processes for Ammonia Production*; 2016; pp 1−30.

(4) Kahrl, F.; Li, Y.; Su, Y.; Tennigkeit, T.; Wilkes, A.; Xu, J. Greenhouse gas emissions from nitrogen fertilizer use in China. *Environmental science & policy* **2010**, *13*, 688−694.

(5) Benchaita, T. *Greenhouse Gas Emissions from New Petrochemical Plants*. Inter-American Development Bank, 2013,.

(6) Lamb, W. F.; Wiedmann, T.; Pongratz, J.; Andrew, R.; Crippa, M.; Olivier, J. G.; Wiedenhofer, D.; Mattioli, G.; Al Khourdajie, A.; House, J. A review of trends and drivers of greenhouse gas emissions by sector from 1990 to 2018. *Environ. Res. Lett.* **2021**, *16*, No. 073005.

(7) Isella, A.; Manca, D. GHG Emissions by (Petro) Chemical Processes and Decarbonization Priorities—A Review. *Energies* **2022**, *15*, 7560.

(8) Schiffer, Z. J.; Manthiram, K. Electrification and decarbonization of the chemical industry. *Joule* **2017**, *1*, 10−14.

(9) Mallapragada, D. S.; Dvorkin, Y.; Modestino, M. A.; Esposito, D. V.; Smith, W. A.; Hodge, B.-M.; Harold, M. P.; Donnelly, V. M.; Nuz, A.; Bloomquist, C.; et al. Decarbonization of the chemical industry through electrification: Barriers and opportunities. *Joule* **2023**, *7*, 23−41.

(10) Fichter, F.; Girard, P.; Erlenmeyer, H. Elektrolytische Bindung von komprimiertem Stickstoff bei gewöhnlicher Temperatur. *Helv. Chim. Acta* **1930**, *13*, 1228−1236.

(11) Suryanto, B. H.; Matuszek, K.; Choi, J.; Hodgetts, R. Y.; Du, H.-L.; Bakker, J. M.; Kang, C. S.; Cherepanov, P. V.; Simonov, A. N.; MacFarlane, D. R. Nitrogen reduction to ammonia at high efficiency and rates based on a phosphonium proton shuttle. *Science* **2021**, *372*, 1187−1191.

(12) Du, H.-L.; Chatti, M.; Hodgetts, R. Y.; Cherepanov, P. V.; Nguyen, C. K.; Matuszek, K.; MacFarlane, D. R.; Simonov, A. N. Electroreduction of nitrogen with almost 100% current-to-ammonia efficiency. *Nature* **2022**, *609*, 722−727.

(13) Li, S.; Zhou, Y.; Li, K.; Saccoccio, M.; Sažinas, R.; Andersen, S. Z.; Pedersen, J. B.; Fu, X.; Shadravan, V.; Chakraborty, D.; et al. Electrosynthesis of ammonia with high selectivity and high rates via engineering of the solid-electrolyte interphase. *Joule* **2022**, *6*, 2083−2101.

(14) Cui, X.; Tang, C.; Zhang, Q. A review of electrocatalytic reduction of dinitrogen to ammonia under ambient conditions. *Adv. Energy Mater.* **2018**, *8*, No. 1800369.

(15) Tsuneto, A.; Kudo, A.; Sakata, T. Efficient electrochemical reduction of N2 to NH3 catalyzed by lithium. *Chemistry letters* **1993**, *22*, 851−854.

(16) Tsuneto, A.; Kudo, A.; Sakata, T. Lithium-mediated electrochemical reduction of high pressure N2 to NH3. *J. Electroanal. Chem.* **1994**, *367*, 183−188.

(17) Fu, X.; Pedersen, J. B.; Zhou, Y.; Saccoccio, M.; Li, S.; Sažinas, R.; Li, K.; Andersen, S. Z.; Xu, A.; Deissler, N. H.; et al. Continuous-flow electrosynthesis of ammonia by nitrogen reduction and hydrogen oxidation. *Science* **2023**, *379*, 707−712.

(18) Lazouski, N.; Chung, M.; Williams, K.; Gala, M. L.; Manthiram, K. Non-aqueous gas diffusion electrodes for rapid ammonia synthesis from nitrogen and water-splitting-derived hydrogen. *Nature Catalysis* **2020**, *3*, 463−469.

(19) McFarlane, E.; Tompkins, F. Nitridation of lithium. *Trans. Faraday Soc.* **1962**, *58*, 997−1007.

(20) Greenwood, N. N.; Earnshaw, A. *Chemistry of the Elements*; Elsevier, 2012; pp 417−420.

(21) Vajenine, G. V. On reactions between alkali metals and active nitrogen. *Solid state sciences* **2008**, *10*, 450−454.

(22) Iriawan, H.; Andersen, S. Z.; Zhang, X.; Comer, B. M.; Barrio, J.; Chen, P.; Medford, A. J.; Stephens, I. E.; Chorkendorff, I.; Shao-Horn, Y. Methods for nitrogen activation by reduction and oxidation. *Nat. Rev. Methods Primers* **2021**, *1*, 56.

(23) Westhead, O.; Barrio, J.; Bagger, A.; Murray, J. W.; Rossmeisl, J.; Titirici, M.-M.; Jervis, R.; Fantuzzi, A.; Ashley, A.; Stephens, I. E. Near ambient N2 fixation on solid electrodes versus enzymes and homogeneous catalysts. *Nature Reviews Chemistry* **2023**, *7*, 184−201.

(24) Cai, X.; Fu, C.; Iriawan, H.; Yang, F.; Wu, A.; Luo, L.; Shen, S.; Wei, G.; Shao-Horn, Y.; Zhang, J. Lithium-mediated electrochemical

nitrogen reduction: Mechanistic insights to enhance performance. *iScience* **2021**, *24*, 1−17.
(25) Singh, A. R.; Rohr, B. A.; Statt, M. J.; Schwalbe, J. A.; Cargnello, M.; Nørskov, J. K. Strategies toward selective electrochemical ammonia synthesis. *ACS Catal.* **2019**, *9*, 8316−8324.
(26) Montoya, J. H.; Tsai, C.; Vojvodic, A.; Nørskov, J. K. The challenge of electrochemical ammonia synthesis: a new perspective on the role of nitrogen scaling relations. *ChemSusChem* **2015**, *8*, 2180−2186.
(27) Kavalsky, L.; Viswanathan, V. Robust active site design of single-atom catalysts for electrochemical ammonia synthesis. *J. Phys. Chem. C* **2020**, *124*, 23164−23176.
(28) Tang, C.; Qiao, S.-Z. How to explore ambient electrocatalytic nitrogen reduction reliably and insightfully. *Chem. Soc. Rev.* **2019**, *48*, 3166−3180.
(29) Pan, J.; Hansen, H. A.; Vegge, T. Vanadium oxynitrides as stable catalysts for electrochemical reduction of nitrogen to ammonia: the role of oxygen. *Journal of Materials Chemistry A* **2020**, *8*, 24098−24107.
(30) Guan, Y.; Liu, C.; Wang, Q.; Gao, W.; Hansen, H. A.; Guo, J.; Vegge, T.; Chen, P. Transition-metal-free barium hydride mediates dinitrogen fixation and ammonia synthesis. *Angew. Chem., Int. Ed.* **2022**, *61*, No. e202205805.
(31) Andersen, S. Z.; Statt, M. J.; Bukas, V. J.; Shapel, S. G.; Pedersen, J. B.; Krempl, K.; Saccoccio, M.; Chakraborty, D.; Kibsgaard, J.; Vesborg, P. C.; et al. Increasing stability, efficiency, and fundamental understanding of lithium-mediated electrochemical nitrogen reduction. *Energy Environ. Sci.* **2020**, *13*, 4291−4300.
(32) Lazouski, N.; Schiffer, Z. J.; Williams, K.; Manthiram, K. Understanding continuous lithium-mediated electrochemical nitrogen reduction. *Joule* **2019**, *3*, 1127−1139.
(33) Chang, W.; Jain, A.; Rezaie, F.; Manthiram, K. Lithium-mediated nitrogen reduction to ammonia via the catalytic solid−electrolyte interphase. *Nat. Catal.* **2024**, 1−11.
(34) Steinberg, K.; Yuan, X.; Klein, C. K.; Lazouski, N.; Mecklenburg, M.; Manthiram, K.; Li, Y. Imaging of nitrogen fixation at lithium solid electrolyte interphases via cryo-electron microscopy. *Nature Energy* **2023**, *8*, 138−148.
(35) Dey, A. Lithium anode film and organic and inorganic electrolyte batteries. *Thin Solid Films* **1977**, *43*, 131−171.
(36) Zhang, Y.; Viswanathan, V. Not All fluorination is the same: Unique effects of fluorine functionalization of ethylene carbonate for tuning solid-electrolyte interphase in Li metal Batteries. *Langmuir* **2020**, *36*, 11450−11466.
(37) Zhang, Y.; Viswanathan, V. Design rules for selecting fluorinated linear organic solvents for li metal batteries. *J. Phys. Chem. Lett.* **2021**, *12*, 5821−5828.
(38) Wang, A.; Kadam, S.; Li, H.; Shi, S.; Qi, Y. Review on modeling of the anode solid electrolyte interphase (SEI) for lithium-ion batteries. *NPJ Comput. Mater.* **2018**, *4*, 15.
(39) Suo, L.; Oh, D.; Lin, Y.; Zhuo, Z.; Borodin, O.; Gao, T.; Wang, F.; Kushima, A.; Wang, Z.; Kim, H.-C.; et al. How solid-electrolyte interphase forms in aqueous electrolytes. *J. Am. Chem. Soc.* **2017**, *139*, 18670−18680.
(40) Li, Y.; Leung, K.; Qi, Y. Computational exploration of the Li-electrode— electrolyte interface in the presence of a nanometer thick solid-electrolyte interphase layer. *Accounts of chemical research* **2016**, *49*, 2363−2370.
(41) Ahmad, Z.; Venturi, V.; Hafiz, H.; Viswanathan, V. Interfaces in solid electrolyte interphase: Implications for lithium-ion batteries. *J. Phys. Chem. C* **2021**, *125*, 11301−11309.
(42) Beltran, S. P.; Balbuena, P. B. SEI formation mechanisms and Li + dissolution in lithium metal anodes: impact of the electrolyte composition and the electrolyte-to-anode ratio. *J. Power Sources* **2022**, *551*, No. 232203.
(43) Tort, R.; Bagger, A.; Westhead, O.; Kondo, Y.; Khobnya, A.; Winiwarter, A.; Davies, B. J.; Walsh, A.; Katayama, Y.; Yamada, Y.; et al. Searching for the Rules of Electrochemical Nitrogen Fixation. *ACS Catal.* **2023**, *13*, 14513−14522.
(44) Shi, S.; Lu, P.; Liu, Z.; Qi, Y.; Hector, L. G., Jr; Li, H.; Harris, S. J. Direct calculation of Li-ion transport in the solid electrolyte interphase. *J. Am. Chem. Soc.* **2012**, *134*, 15476−15487.
(45) Angarita-Gomez, S.; Balbuena, P. B. Lithium-Ion Transport through Complex Interphases in Lithium Metal Batteries. *ACS Appl. Mater. Interfaces* **2022**, *14*, 56758−56766.
(46) Krishnamurthy, D.; Lazouski, N.; Gala, M. L.; Manthiram, K.; Viswanathan, V. Closed-loop electrolyte design for lithium-mediated ammonia synthesis. *ACS Central Science* **2021**, *7*, 2073−2082.
(47) Lazouski, N.; Steinberg, K. J.; Gala, M. L.; Krishnamurthy, D.; Viswanathan, V.; Manthiram, K. Proton donors induce a differential transport effect for selectivity toward ammonia in lithium-mediated nitrogen reduction. *ACS Catal.* **2022**, *12*, 5197−5208.
(48) Fu, X.; Xu, A.; Pedersen, J. B.; Li, S.; Sažinas, R.; Zhou, Y.; Andersen, S. Z.; Saccoccio, M.; Deissler, N. H.; Mygind, J. B. V. Phenol as proton shuttle and buffer for lithium-mediated ammonia electrosynthesis. *Nat. Commun.* **2024**, *15*, 2417.
(49) Mortensen, J. J.; Hansen, L. B.; Jacobsen, K. W. Real-space grid implementation of the projector augmented wave method. *Phys. Rev. B* **2005**, *71*, No. 035109.
(50) Enkovaara, J.; Rostgaard, C.; Mortensen, J. J.; Chen, J.; Dułak, M.; Ferrighi, L.; Gavnholt, J.; Glinsvad, C.; Haikola, V.; Hansen, H.; et al. Electronic structure calculations with GPAW: a real-space implementation of the projector augmented-wave method. *J. Phys.: Condens. Matter* **2010**, *22*, 253202.
(51) Kavalsky, L.; Hegde, V. I.; Meredig, B.; Viswanathan, V. A multiobjective closed-loop approach towards autonomous discovery of electrocatalysts for nitrogen reduction. *Digital Discovery* **2024**, *3*, 999−1010.
(52) Himanen, L.; Jäger, M. O. J.; Morooka, E. V.; Federici Canova, F.; Ranawat, Y. S.; Gao, D. Z.; Rinke, P.; Foster, A. S. DScribe: Library of descriptors for machine learning in materials science. *Comput. Phys. Commun.* **2020**, *247*, No. 106949.
(53) Laakso, J.; Himanen, L.; Homm, H.; Morooka, E. V.; Jäger, M. O.; Todorović, M.; Rinke, P. Updates to the DScribe library: New descriptors and derivatives. *J. Chem. Phys.* **2023**, *158*, 234802.
(54) De, S.; Bartók, A. P.; Csányi, G.; Ceriotti, M. Comparing molecules and solids across structural and alchemical space. *Phys. Chem. Chem. Phys.* **2016**, *18*, 13754−13769.
(55) Jäger, M. O.; Morooka, E. V.; Federici Canova, F.; Himanen, L.; Foster, A. S. Machine learning hydrogen adsorption on nanoclusters through structural descriptors. *npj Comput. Mater.* **2018**, *4*, 37.
(56) Bartók, A. P.; Kondor, R.; Csányi, G. On representing chemical environments. *Phys. Rev. B* **2013**, *87*, No. 184115.
(57) Willatt, M. J.; Musil, F.; Ceriotti, M. Feature optimization for atomistic machine learning yields a data-driven construction of the periodic table of the elements. *Phys. Chem. Chem. Phys.* **2018**, *20*, 29661−29668.
(58) Faber, F.; Lindmaa, A.; Von Lilienfeld, O. A.; Armiento, R. Crystal structure representations for machine learning models of formation energies. *Int. J. Quantum Chem.* **2015**, *115*, 1094−1101.
(59) Sainburg, T.; McInnes, L.; Gentner, T. Q. Parametric UMAP Embeddings for Representation and Semisupervised Learning. *Neural Comput.* **2021**, *33*, 2881−2907.
(60) McInnes, L.; Healy, J.; Astels, S. hdbscan: Hierarchical density based clustering. *J. Open Source Software* **2017**, *2*, 1.
(61) Pande, V.; Viswanathan, V. Computational screening of current collectors for enabling anode-free lithium metal batteries. *ACS Energy Letters* **2019**, *4*, 2952−2959.
(62) Tyson, W. R.; Miller, W. A. Surface free energies of solid metals: Estimation from liquid surface tension measurements. *Surf. Sci.* **1977**, *62*, 267−276.
(63) Phuthi, M. K.; Yao, A. M.; Batzner, S.; Musaelian, A.; Guan, P.; Kozinsky, B.; Cubuk, E. D.; Viswanathan, V. Accurate Surface and Finite-Temperature Bulk Properties of Lithium Metal at Large Scales Using Machine Learning Interaction Potentials. *ACS omega* **2024**, *9*, 10904−10912.

https://doi.org/10.1021/acs.jpcc.4c08138
J. Phys. Chem. C 2025, 129, 2488−2501

(64) Azofra, L. M.; Dona-Rodriguez, J. M.; MacFarlane, D. R.; Simonov, A. N. Mechanism of the N2 Cleavage Promoted by Lithium vs Other Alkali and Alkaline-Earth Metals. *J. Phys. Chem. C* **2024**, 1−8.
(65) Gregory, D. H. Nitride chemistry of the s-block elements. *Coord. Chem. Rev.* **2001**, *215*, 301−345.
(66) Alpen, U. Li3N: A promising Li ionic conductor. *J. Solid State Chem.* **1979**, *29*, 379−392.
(67) Zintl, E.; Brauer, G. Konstitution des lithiumnitrids. *Zeitschrift f ü r Elektrochemie und angewandte physikalische Chemie* **1935**, *41*, 102−107.
(68) Ludwig, T.; Singh, A. R.; Nørskov, J. K. Subsurface nitrogen dissociation kinetics in lithium metal from metadynamics. *J. Phys. Chem. C* **2020**, *124*, 26368−26378.
(69) Tsiverioti, L. M.; Kavalsky, L.; Viswanathan, V. Robust analysis of 4e−versus 6e−reduction of nitrogen on metal surfaces and single-atom alloys. *J. Phys. Chem. C* **2022**, *126*, 12994−13003.
(70) Houchins, G.; Krishnamurthy, D.; Viswanathan, V. The role of uncertainty quantification and propagation in accelerating the discovery of electrochemical functional materials. *MRS Bull.* **2019**, *44*, 204−212.
(71) McInnes, L.; Healy, J.; Saul, N.; Großberger, L. UMAP: Uniform Manifold Approximation and Projection. *Journal of Open Source Software* **2018**, *3*, 861.
(72) Fu, X.; Niemann, V. A.; Zhou, Y.; Li, S.; Zhang, K.; Pedersen, J. B.; Saccoccio, M.; Andersen, S. Z.; Enemark-Rasmussen, K.; Benedek, P.; et al. Calcium-mediated nitrogen reduction for electrochemical ammonia synthesis. *Nat. Mater.* **2024**, *23*, 101−107.
(73) Tang, W.; Sanville, E.; Henkelman, G. A grid-based Bader analysis algorithm without lattice bias. *J. Phys.: Condens. Matter* **2009**, *21*, No. 084204.
(74) Yokoyama, T.; Taft, R.; Kamlet, M. J. The solvatochromic comparison method. 3. Hydrogen bonding by some 2-nitroaniline derivatives. *J. Am. Chem. Soc.* **1976**, *98*, 3233−3237.
(75) Kamlet, M. J.; Taft, R. The solvatochromic comparison method. I. The. beta.-scale of solvent hydrogen-bond acceptor (HBA) basicities. *Journal of the American chemical Society* **1976**, *98*, 377−383.
(76) Taft, R.; Kamlet, M. J. The solvatochromic comparison method. 2. The. alpha.-scale of solvent hydrogen-bond donor (HBD) acidities. *J. Am. Chem. Soc.* **1976**, *98*, 2886−2894.
(77) Reichardt, C.; Welton, T. *Solvents and Solvent Effects in Organic Chemistry*; John Wiley & Sons, 2011; pp 93−96.
(78) Gutmann, V. Empirical parameters for donor and acceptor properties of solvents. *Electrochim. Acta* **1976**, *21*, 661−670.
(79) Gutmann, V.; Resch, G. The Impact of the Donor-Acceptor Concept. *Comments on Inorganic Chemistry* **1982**, *1*, 265−278.
(80) Reichardt, C. Empirical parameters of the polarity of solvents. *Angewandte Chemie International Edition in English* **1965**, *4*, 29−40.
(81) Haak, J. R.; Engberts, J. B. Solvent polarity and solvation effects in highly aqueous mixed solvents. Application of the Dimroth-Reichardt ET (30) parameter. *Recueil des Travaux Chimiques des Pays-Bas* **1986**, *105*, 307−311.
(82) Lofthus, A.; Krupenie, P. H. The spectrum of molecular nitrogen. *Journal of physical and chemical reference Data* **1977**, *6*, 113−307.
(83) Kukushkin, V. Y.; Pombeiro, A. J. Metal-mediated and metal-catalyzed hydrolysis of nitriles. *Inorg. Chim. Acta* **2005**, *358*, 1−21.
(84) Krieble, V. K.; Noll, C. I. The hydrolysis of nitriles with acids. *J. Am. Chem. Soc.* **1939**, *61*, 560−563.
(85) Magat, E. E.; Faris, B. F.; Reith, J. E.; Salisbury, L. F. Acid-catalyzed reactions of nitriles. I. The reaction of nitriles with formaldehyde1. *J. Am. Chem. Soc.* **1951**, *73*, 1028−1031.
(86) Tewari, Y. B.; Goldberg, R. N. Thermodynamics of the hydrolysis reactions of nitriles. *J. Chem. Thermodyn.* **2005**, *37*, 720−728.
(87) Wade, L.; Simek, W. *Organic Chemistry*, 10th ed.; Pearson, 2022; pp 1135−1136.
(88) Fleming, F. F.; Zhang, Z.; Liu, W.; Knochel, P. Metalated Nitriles: Organolithium,-magnesium, and-copper Exchange of α-Halonitriles. *Journal of Organic Chemistry* **2005**, *70*, 2200−2205.
(89) Elangovan, S.; Topf, C.; Fischer, S.; Jiao, H.; Spannenberg, A.; Baumann, W.; Ludwig, R.; Junge, K.; Beller, M. Selective catalytic hydrogenations of nitriles, ketones, and aldehydes by well-defined manganese pincer complexes. *J. Am. Chem. Soc.* **2016**, *138*, 8809−8814.
(90) Wade, L.; Simek, W. *Organic Chemistry*, 10th ed.; Pearson, 2022; pp 949−950.
(91) Swain, C. G. The Mechanism of Addition of Grignard Reagents to Nitriles. *J. Am. Chem. Soc.* **1947**, *69*, 2306−2309.
(92) Blicke, F.; Tsao, E.-P. The Reaction of Certain Nitriles with Grignard Reagents1. *J. Am. Chem. Soc.* **1953**, *75*, 5587−5590.
(93) Kamlet, M. J.; Abboud, J. L.; Taft, R. The solvatochromic comparison method. 6. The. pi.* scale of solvent polarities. *J. Am. Chem. Soc.* **1977**, *99*, 6027−6038.

https://doi.org/10.1021/acs.jpcc.4c08138
J. Phys. Chem. C 2025, 129, 2488−2501